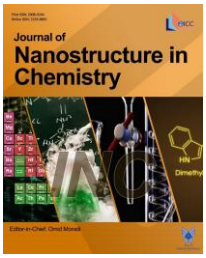

Volume 15, Issue 6, 152525 (1-19)

Journal of Nanostructure in Chemistry (JNSC)

https://doi.org/10.57647/jnsc.2025.1506.25

Anion-Engineered Cobalt Salts as Exogenous Modulators for Phase Tailoring in $CsPbBr_3$ Nanocrystals: Minimal Doping Towards Enhanced Color Fidelity, and Stable White LEDs

Hairong Zhao[1], Anxin Shuai[2], Ran Huang[2], Kaliyamoorthy Justice Babu[3], Muhammad Moin[1], Chengjie Wang[1], Mehrunisa Moin[1], Sonu Kumar[1], Indra Neel Pulidindi[4], Arup Neogi[1], Yixi Wang[2,*], Marek Piotrowski,[1,*], Udayabhaskararao Thumu[1,*]

[1]*Institute of Fundamental and Frontier Sciences, University of Electronic Science and Technology of China, Chengdu 610054, China*

[2]*School of New Energy Materials and Chemistry, Leshan Normal University, Leshan, Sichuan 614000, China*

[3]*Institute of Nano Science and Technology, Mohali, Punjab 140306, India*

[4]*Saveetha Institute of Medical and Technical Sciences (SIMATS), Thandalam, Chennai, 602105, India*

[*]**Corresponding authors:** wangyixi301@163.com, marek@uestc.edu.cn, uday@uestc.edu.cn

Original Research

Received:
1 August 2025

Revised:
15 September 2025

Accepted:
28 September 2025

Published in Issue:
31 December 2025

Abstract

Doping colloidal $CsPbBr_3$ perovskite nanocrystals (NCs) provides an effective strategy to enhance their optoelectronic properties and expand their application potential in display technologies, enabling high color fidelity (Rf) in white-LEDs (WLEDs). Although an excess of Pb^{2+} is known to promote phase-pure and emissive $CsPbBr_3$ NCs, the influence of exogenous dopant precursor chemistry—particularly the counter-anion and the metal ion-to-lead ratio remains poorly understood. In this work, we systematically investigate cobalt precursor identity and Pb: Co feed ratios in Co:$CsPbBr_3$ NCs synthesized by hot injection. Three cobalt salts—$CoBr_2$ (^{b}Co), $Co(CH_3COO)_2$ (^{a}Co), and $Co(NO_3)_2$ (^{n}Co), were investigated (0.16–3.35 at% doping). Among the ^{b}Co produced the best results, retaining the perovskite phase and high photoluminescence (~60%) at low loading, while ^{a}Co and ^{n}Co induced non-emissive Cs_4PbBr_6 formation, and high ^{b}Co loading led to nanosheet morphologies. In WLEDs, ^{b}Co:$CsPbBr_3$ (8:2) demonstrated high color accuracy, superior stability compared to pristine and other doped NCs. Importantly, ^{b}Co:$CsPbBr_3$ retained ~92% of its initial color fidelity over 10 minutes, whereas pristine $CsPbBr_3$ retained only ~78%. Moreover, the WLEDs exhibited a wide color gamut (~122.9% NTSC, ~91.7% Rec. 2020), highlighting the crucial role of dopant precursor selection in optimizing phase stability, doping efficiency, and device performance.

Keywords: Anion effect; Cesium lead bromide; Cobalt precursors; Doping; White light-emitting diodes (WLEDs)

Cite this article: Zhao, H., Anxin, Sh., Huang, R., Justice Babu, K., Moin, M., Wang, Ch., Moin, M., Kumar, S., Neel Pulidindi, I., Neogi, A., Wang, Y., Piotrowski, M., Thumu, U Anion-Engineered Cobalt Salts as Exogenous Modulators for Phase Tailoring in $CsPbBr_3$ Nanocrystals: Minimal Doping Towards Enhanced Color Fidelity, and Stable White LEDs. *J Nanostruct Chem* **15**(06), 152525 (2025).

1. Introduction

Metal halide perovskite nanocrystals (NCs), particularly $CsPbBr_3$, have attracted significant attention for next-generation optoelectronics due to their high photoluminescence quantum yields (PLQY), narrow emission linewidths, and compositional tunability [1, 2]. Their sharp emissive features provide excellent color purity and fidelity, which are essential for high-performance display technologies. The increasing demand for wide color-gamut backlight units in smartphones, monitors, and televisions has highlighted $CsPbBr_3$ NCs as promising candidates [3]. In addition to display applications, these NCs are also suitable for optical waveguides [4-6], solid-state lighting WLEDs [7], and information storage devices [8, 9]. However, the ability to reproducibly access monodisperse, phase-pure $CsPbBr_3$ NCs with optimal optical characteristics remains tightly coupled to synthetic control, particularly concerning ligand dynamics [10, 11], precursor selection [12], and reaction stoichiometry [13,14,15]. For example, Manna *et al.* synthesized $CsPbBr_3$ NCs with varied morphologies, 1D nanorods, 2D nanoplatelets, 3D nanocubes, and quantum dots (QDs) - depending on the lead source (acetate, bromide, oxide, or nitrate) by using diethyl 2-bromomalonate as the bromide precursor [12, 14]. Additionally, in the conventional synthesis of $CsPbBr_3$ NCs, CsOA reacts with $PbBr_2$ ($2CsOA+3PbBr_2 \rightarrow 2CsPbBr_3+PbOA$), and excess Pb salts are typically required to ensure complete perovskite formation. Hence, the use of over stoichiometric Pb^{2+} - with a Cs: Pb ratio typically set at 1:2 or lower has emerged as an ongoing need for achieving uniform cubic NCs. While this strategy ensures complete Cs^+ consumption, it invariably results in excess unreacted Pb^{2+} in the growth medium, raising concerns over toxicity and colloidal instability[15]. A rational alternative is to partially substitute this excess Pb^{2+} with other divalent cations, introducing the "exogenous" ions. Such substitution not only offers a route to reducing lead content but also enables functional modulation of structural and photophysical properties. Among the various dopants investigated, transition metal ions, including Zn^{2+}, Hg^{2+}, Cu^{2+}, Ni^{2+}, Mn^{2+}, and non-transition metal species like In^{3+}, Al^{3+}, Sn^{4+}, Mg^{2+}, Ca^{2+}, Ba^{2+}, and Na^+, have shown notable promise in enhancing the robustness and emission characteristics of the perovskite.

Apart from the toxicity, the metal cations, doping serves as an effective method to contribute to various stabilization strategies to overcome the inherent instability, leading to enhancement in the optical properties. Successful examples include doping with Fe, Ni, Co, Zn, Mn, Sn, Sr, Cr, Li and various lanthanides, each contributing to improved durability and tunable emission characteristics [16-19].

In particular, Co^{2+}, an earth-abundant and environmentally benign dopant, was extensively used for producing composite materials for various energy applications [20-22]. Co^{2+} has demonstrated potential for the partial substitution at the Pb^{2+} in the perovskite lattice, thereby improving both the material stability and optoelectronic performance [18, 19]. For instance, Babeker *et al.* reported creating Co-doped $CsPbI_3$ NC exhibiting tunable emission from 702 to 652 nm, and their thermal stability was substantially improved when introduced to glasses [18]. Similarly, Wang *et al.* achieved a notable increase in power conversion efficiency (8.57 %) in Co-doped $CsPbBr_3$ films compared to undoped counterparts (6.81 %), confirming the potential of Co^{2+} incorporation to boost device performance [19].

However, most of these studies have employed a single cobalt precursor, with limited insight into how precursor chemistry—especially the identity of the accompanying anion—influences dopant incorporation, phase evolution, and photoluminescence behavior. Emerging reports have begun to highlight how the precursor anion influences doping behavior. Cheng *et al.*, for example, utilized acetate-modified $CsPbBr_3$ NCs to enable efficient Ni^{2+} doping, enhancing the photocatalytic CO_2 reduction activity [23]. Yet, a systematic understanding of how different anions—such as acetate, bromide, or nitrate— in the dopant precursor affect the dopant (Co^{2+}) incorporation, phase evolution, and optical performance in doped $CsPbBr_3$ NCs was lacking in the existing literature.

Herein, we report a systematic investigation into the role of exogenous ions in perovskite nanocrystals, focusing on how the counteranions of cobalt precursors—Co $(CH_3COO)_2$ (^{a}Co), $CoBr_2$ (^{b}Co), and $Co(NO_3)_2$ (^{n}Co)—govern Co^{2+} doping in $CsPbBr_3$ nanocrystals synthesized via the hot-injection method. The combined effects of the precursor anion and the Pb:Co feeding ratio on doping efficiency, phase stability, and photoluminescence behavior were systematically examined. At lower Co^{2+} concentrations ($PbBr_2$: ^{b}Co =3:7), doping maintains the ^{b}Co: $CsPbBr_3$ perovskite phase and enhances PL intensity. In contrast, excessive Co^{2+} loading ($PbBr_2$: ^{b}Co = 2:8) results in mixed morphologies, including ^{b}Co:$CsPbBr_3$ NCs and nanosheets (NSs), along with a

minor presence of the rhombohedral Cs_4PbBr_6 phase. This is accompanied by reduced PL emission and the emergence of a new absorption feature at 317 nm. Notably, with alternative Co precursors, optically active $CsPbBr_3$ NCs emerge at lower ^{n}Co and ^{a}Co feed ratios but transform into non-emissive Cs_4PbBr_6 at higher loadings, emphasizing the subtle yet crucial role of the counter anion in directing phase evolution and optical properties. Among all systems, ^{b}Co:$CsPbBr_3$ NCs exhibit the most favorable balance of PL enhancement (~ 60 %) and long-term structural stability. These doped NCs were further integrated into the white light-emitting diodes (WLEDs), achieving a fidelity ratio (Rf) value of 67.2 and color gamut (at 20 mA) coverage of 122.9 % (NTSC) and 91.7 % (Rec. 2020), demonstrating their promise for display technologies. Overall, this work provides a new insight into the importance of dopant precursor chemistry, particularly the identity of the counter anion, in controlling the dopant incorporation, phase behavior, and optoelectronic performance in Co-doped perovskite NCs.

2. Materials and Methods

2.1. Experimental details

2.1.1. *Materials*

$PbBr_2$, $CoBr_2 \cdot 2H_2O$, Co $(NO_3)_2$, Co $(OAc)_2 \cdot 4H_2O$, cesium carbonate (Cs_2CO_3), hexane, octadecene (ODE), methyl acetate (analytical reagent, AR), oleic acid (OA), and oleylamine (OLAM) were purchased from Sigma-Aldrich. All the chemical reagents were used as received without further purification.

2.1.2. *Preparation of Cs-oleate (Cs-OA)*

Cs_2CO_3 (0.814 g) was loaded into a 100 mL 3-neck flask along with ODE (40 mL) and OA (2.5 mL) and stirred for 1 h at 120 °C under vacuum conditions, and then heated under Argon to 150 °C until all Cs_2CO_3 reacted with OA. Finally, the resulting solution was cooled to room temperature and stored in the refrigerator for further use.

2.1.3. *Synthesis of $CsPbBr_3$ NCs*

$PbBr_2$ (0.069 g) was added to 5 mL ODE in a flask on a hotplate set at 120 °C. Note that $PbBr_2$ is insoluble in ODE. After 1 h of stirring under vacuum, 0.5 mL OA and 0.5 mL OLAM were injected simultaneously. This step facilitates the dissolution of $PbBr_2$, resulting in the formation of a clear solution, indicating successful complexation of $PbBr_2$ with the ligands. The reaction temperature was then increased to 150 °C under a nitrogen gas atmosphere. Subsequently, 0.4 mL of Cs-OA solution was injected into the reaction mixture. The reaction mixture was then quickly cooled down by immersing the flask in ice-cold water until it reached room temperature. The resulting NCs were collected and stored in the refrigerator for further studies.

2.1.4. *Synthesis of ^{b}Co:$CsPbBr_3$ NCs, ^{n}Co:$CsPbBr_3$ NCs and ^{a}Co:$CsPbBr_3$ NCs*

For the synthesis of Co^{2+} doped $CsPbBr_3$ NCs, different amounts of ^{b}Co salts were added (^{b}Co contents ranging from 10, 20, 30, 40, 50, 60, 70 to 80%, changing the mole ratio of $PbBr_2$, the total $PbBr_2$ amount is 0.188 mmol) to 5 mL ODE. For the cases, using ^{a}Co and ^{n}Co as Co^{2+} precursors, the same synthesis procedure was followed, except that the ^{b}Co is replaced with ^{a}Co and ^{n}Co. Other synthesis steps were the same as those used for producing pure $CsPbBr_3$ NCs. The as-prepared $CsPbBr_3$ and Co doped counterparts (Co: $CsPbBr_3$ NCs) obtained using different Co^{2+} precursors were washed with methyl acetate using centrifugation at 8500 rpm for 5 min. The resulting solid materials were then dissolved in hexane for further characterization.

2.2. Characterization techniques

2.2.1. *Measurement of optical properties*

Ultraviolet-visible (UV-vis) absorption spectra were recorded using the Shimadzu UV-1900 Spectrophotometer. Several individual reaction vials were prepared and the spectra were recorded under consistent dilution conditions. The PL spectra were measured using the Hitachi F-4700 fluorescence spectrophotometer. The total volume of each of the samples was approximately 2 mL. For each PL measurement, the reaction solution was used as it was, without further dilution. PLQY measurements were conducted using Rhodamine B (RhB) as a reference standard [24].

2.2.2. *Ultrafast transient absorption (TA) analysis*

The ultrafast transient absorption (TA) spectroscopy was recorded by using a Harpia-TA (Light Conversion) transient absorption spectrometer. The pump and probe beams were derived from the 1030

nm PHAROS femtosecond lasers (200 uJ pulse^{-1},50 Khz,~110 fs, Light Conversion). The pump pulse was generated by output pulse 1030 nm, which was directly into the optical parametric amplifier (OPA, Orpheus-HP, Light Conversion) to get 365 nm as a pump pulse to excite samples. The supercontinuous white light probe was generated by focusing a 515 nm second-harmonic beam onto sapphire.

2.2.3. *Time-resolved photoluminescence (TRPL) analysis*

The time-resolved spectroscopy was recorded by HARPIA-TF (Light conversion). Time-correlated single photon counting (TCSPC) module. The samples were excited at 365 nm.

2.2.4. *High-resolution transmission electron microscopy (HR-TEM) analysis*

The structure of the prepared Co:$CsPbBr_3$ NCs was analyzed by using a high-resolution transmission electron microscope (HR-TEM, 200 kV TECNAI G2 F20 equipped with a Gatan SC200 CCD camera, FEI, USA).

2.2.5. *X-ray diffraction (XRD) patterns*

XRD patterns of NCs (pure and Co doped systems) were measured with a D2 PHASER desktop diffractometer (Bruker, Germany), utilizing a Cu Kα source.

2.2.6. *X-ray photoelectron spectroscopy (XPS) analysis*

X-ray photoelectron spectroscopy (XPS) patterns were measured with a Thermo Scientific K-Alpha instrument, employing Al Kα radiation (hν = 1486.6 eV) as the excitation source.

2.2.7. *Density functional theory (DFT)*

In this investigation, all computational studies were performed employing the Cambridge serial total energy package (CASTEP) code within the Materials Studio, based on the density functional theory (DFT) with a plane-wave pseudopotential technique. The exchange-correlation interactions were treated using the generalized gradient approximation (GGA) as parameterized by Perdew, Burke, and Ernzerhof (PBE). A plane-wave energy cut-off of 480 eV/atom was applied, and the self-consistent field (SCF) convergence criterion was strictly maintained throughout.

To perfect the interaction that exists between valence electrons and atomic cores, ultrasoft pseudopotentials were used. A plane-wave energy cut-off of 480 eV/atom was applied, and the self-consistent field (SCF) convergence criterion was strictly maintained throughout. For systems optimization, the pristine $CsPbBr_3$ and Co^{2+}-substituted $CsPb_{1-x}Co_xBr_3$ (cubic phase, space group $Pm\bar{3}m$) systems were relaxed after using Monkhorst–Pack k-point mesh of 10 × 10 × 10. The geometry optimization of all systems was considered complete when the following criteria were met: energy tolerance, maximum stress of 0.02 GPa, maximum force of 0.01 eV/Å, and a maximum atomic displacement of 5.0×10^{-4} Å. The resulting band gap value for the pristine $CsPbBr_3$ system matched well with experimental observations, confirming the reliability of the computational parameters.

2.2.8. *Preparation of WLEDs*

White light-emitting devices were fabricated through a phosphor-conversion approach using optimized Co-doped $CsPbBr_3$ nanocrystals as the green emitter, commercial $K_2SiF_6:Mn^{4+}$ as the red emitter, and a 1 W blue LED chip (λ ≈ 455 nm, San'an Optoelectronics) as the excitation source. These powders were mixed in an approximate mass ratio (sample powder and red powder) of 10:1. Finally, UV curable adhesive was used to blend the powder and adhesive in a 1:1 mass ratio (referring to the total mass of all powder mixtures). The LED chip utilized was of 1 W, with a wavelength of approximately 455 nm and was provided by San'an Optoelectronics Co., Ltd. Subsequently, tests were carried out by varying the current from 10 mA to 320 mA to obtain the white light-emitting PL spectra.

3. Results and Discussion

The synthesis of Co:$CsPbBr_3$ NCs was carried out using a typical hot injection method, where ^{b}Pb was mixed with oleic acid and oleylamine together with different types of cobalt salts (^{b}Co, ^{n}Co, ^{a}Co), as illustrated schematically in Fig. 1a. The selection of halides, acetate, and nitrate anions was based on their widespread use, cost-effectiveness, and representative chemical functionalities relevant to NC's surface chemistry and coordination behavior. These three represent major chemical properties, such as halides for part of the lattice, acetate for a chelating agent, and

nitrate for the small reactive molecules. The systematic variation in the Pb/Co molar ratio (8:2-2:8) during the hot-injection synthesis of Cs-Pb-Br NCs had a notable impact on their optical properties, as shown in Fig. 1b-d. As shown in Fig. 1b, in the case of the ^{b}Co (Br^- anion), the formation of optically active Co-doped $CsPbBr_3$ is favored at a ^{b}Pb:^{b}Co ratio of 8:2 until 2:8. With further increase in the ^{b}Pb:^{b}Co feeding ratio (2:8), three types of mixed structures were seen in the reaction mixture, namely, the $CsPbBr_3$ NCs, $CsPbBr_3$ NSs and Cs_4PbBr_6 NCs. In the case of ^{a}Co (CH_3COO^- anion), at a feeding ratio ^{b}Pb:^{a}Co=8:2, the $CsPbBr_3$ NCs are formed. This means that its phase is stable under these synthetic conditions. However, at a ^{b}Pb:^{a}Co ratio of 5:5, the reaction mixture yields a mixed phase of $CsPbBr_3$ and Cs_4PbBr_6 NCs, with the latter being the dominant product. With further increase in the feeding ratio (3:7), no more Co-$CsPbBr_3$ NCs were seen but the reaction medium is dominated by the formation of the non-emissive Cs_4PbBr_6 phase, as shown in Fig. 1c. For the ^{n}Co (NO_3^- anion) case, $CsPbBr_3$ is formed only at ^{b}Pb:^{n}Co = 8:2. Further increasing the amount of ^{n}Co led to the formation of the Cs_4PbBr_6 phase, ultimately, to degradation, as shown in Fig. 1d.

The choice of cobalt precursor during the hot-injection synthesis of Co-doped $CsPbBr_3$ nanocrystals significantly influences their optical properties, as revealed by the UV–vis absorption and photoluminescence (PL) spectra (Fig. 2). Fig. 2a shows the changes in the absorption spectra while varying the ^{b}Pb:^{b}Co feed ratio (8:2 to 2:8) when using ^{b}Co as the precursor. A strong absorption band at 520 nm was observed for NCs prepared with a ^{b}Pb:^{b}Co ratio from 8:2 to 3:7, while with further increase in the ^{b}Co in the reaction mixture, at a 2:8 ratio, an additional band at 317 nm was observed which was attributed to the Cs_4PbBr_6 phase.

Fig. 2a shows the orange dotted line corresponding to undoped $CsPbBr_3$, with a band at 520 nm matching the orthorhombic phase. The $CoBr_2$, exhibiting two peaks at 550 nm and 700 nm (Fig. S1). Co-doped $CsPbBr_3$ follows a similar trend to undoped $CsPbBr_3$ NCs, and the absence of additional peaks indicates that no absorption features from intrinsic Co^{2+} are present. The coexistence of both the bands at 520 nm and 317 nm indicates the presence of both the $CsPbBr_3$ and Cs_4PbBr_6 NCs (confirmed by TEM analysis as well which was discussed in the subsequent sections).

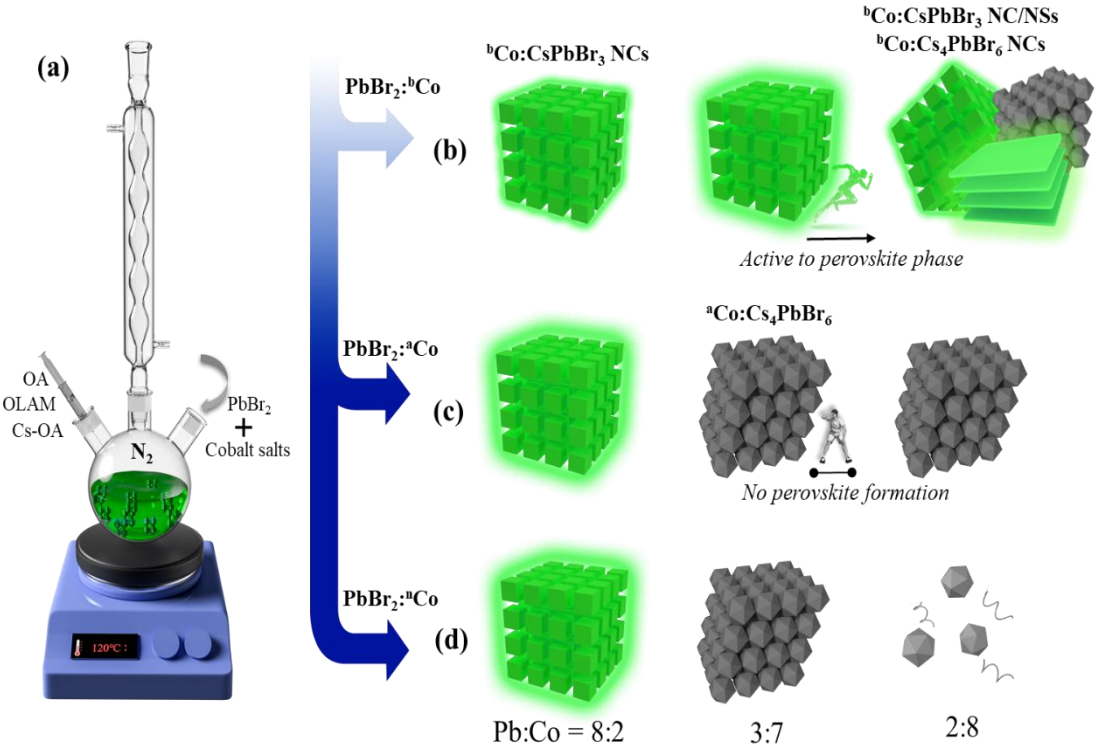

Figure 1. (a) Schematic illustration of the hot-injection synthesis of Co:$CsPbBr_3$ NCs using three different cobalt precursors: ^{b}Co, ^{n}Co, and ^{a}Co. The Pb: Co feed ratios are varied as indicated (8:2, 3:7, 2:8). (b–d) Evolution of $CsPbBr_3$ and Cs_4PbBr_6 NCs during the reaction upon doping with (b) ^{b}Co, (c) ^{a}Co, and (d) ^{n}Co, respectively. A progressive phase change from green-emissive $CsPbBr_3$ to non-emissive Cs_4PbBr_6 is observed, depending on the type and concentration of the Co precursor. [OA – oleic acid; OLAM – oleylamine; Cs-OA – cesium oleate]

With an increase in the feeding ratio, the PL emission undergoes a slight red shift from 517 nm to 522 nm, which is related to the cobalt-doping and changes in morphology and crystal phase (Fig. 2d).

At the highest Co doping concentration reduces the band gap, as confirmed by our DFT calculations, from 2.88 eV in pristine $CsPbBr_3$ to 1.8 eV in Co-doped systems (see later section). Maximum shift notices for ^{b}Co:$CsPbBr_3$ NCs (4:6) from 517 nm to 524 nm, corresponding to higher Co incorporation (3.35 at%). Further increasing the Co content (^{b}Pb:^{b}Co = 3:7 and 2:8) results in a slight blue shift (~522 nm), likely due to structural changes such as nanoplatelet formation or phase transformations that affect the photoluminescence behavior. The PL intensity increases upon ^{b}Co doping of $CsPbBr_3$ NCs, reaching a maximum at a ^{b}Pb:^{b}Co ratio of 8:2, but decreases with further addition of ^{b}Co. This decline in PL intensity is attributed to the reduced Pb content in the original reaction mixture, which likely induces structural defects in the NCs. The lowest PL emission observed for the NCs solution synthesized at a reduced ^{b}Pb:^{a}Co feed ratio of 2:8 is attributed to the coexistence of mixed morphologies and phases, specifically $CsPbBr_3$ and non-emissive Cs_4PbBr_6 NCs. These results indicate that optimal PL emission occurs at a ^{b}Pb:^{b}Co ratio of 8:2 (Fig. 2d). In the second case, ^{a}Co was employed as the cobalt precursor for doping under the same synthetic conditions, with varying ^{b}Pb:^{a}Co molar ratios. At a ^{b}Pb:^{a}Co ratio of 8:2, the ^{a}Co:$CsPbBr_3$ NCs exhibit a weak absorption feature at ~520 nm, characteristic of the orthorhombic $CsPbBr_3$ phase. As the Co^{2+} precursor concentration increases (^{b}Pb:^{a}Co ratios 5:5, 4:6, 3:7, to 2:8), an additional absorption peak emerges at 317 nm, while the 520 nm feature gradually weakens and eventually disappears at the highest ^{a}Co loading (2:8) (Fig. 2b) [25]. This trend indicates the progressive loss of ^{a}Co:$CsPbBr_3$ NCs and a concurrent increase in the formation of Cs_4PbBr_6 NCs with higher ^{a}Co feeding. The associated PL spectra (Fig. 2e) show a rapid decline in emission intensity, attributed to the increasing dominance of the non-emissive Cs_4PbBr_6 phase. In the third case, ^{n}Co was used as the Co^{2+} precursor for synthesizing ^{n}Co:$CsPbBr_3$ NCs, employing the same ^{b}Pb:^{n}Co molar ratios (8:2, 5:5, 4:6, 3:7, and 2:8). As shown in Fig. 2c, a strong absorption peak at ~520 nm was observed for samples with ratios 8:2, 5:5, 4:6, and 3:7, indicative of retained $CsPbBr_3$ phase. Upon reaching the ratio of 3:7, a new absorption peak at 317 nm appeared, suggesting the onset of Cs_4PbBr_6 formation. Notably, the 2:8 sample exhibited no distinct absorption features, indicating the absence of both phases. Notably, the NCs synthesized beyond the 8:2 ratio were highly unstable and decomposed within hours, with potential causes discussed in later sections. Consistent with the UV–vis absorption profile and the increasing presence of non-emissive Cs_4PbBr_6 NCs, the PL intensity declined markedly from 8:2 to 3:7, as shown in Fig. 2f.

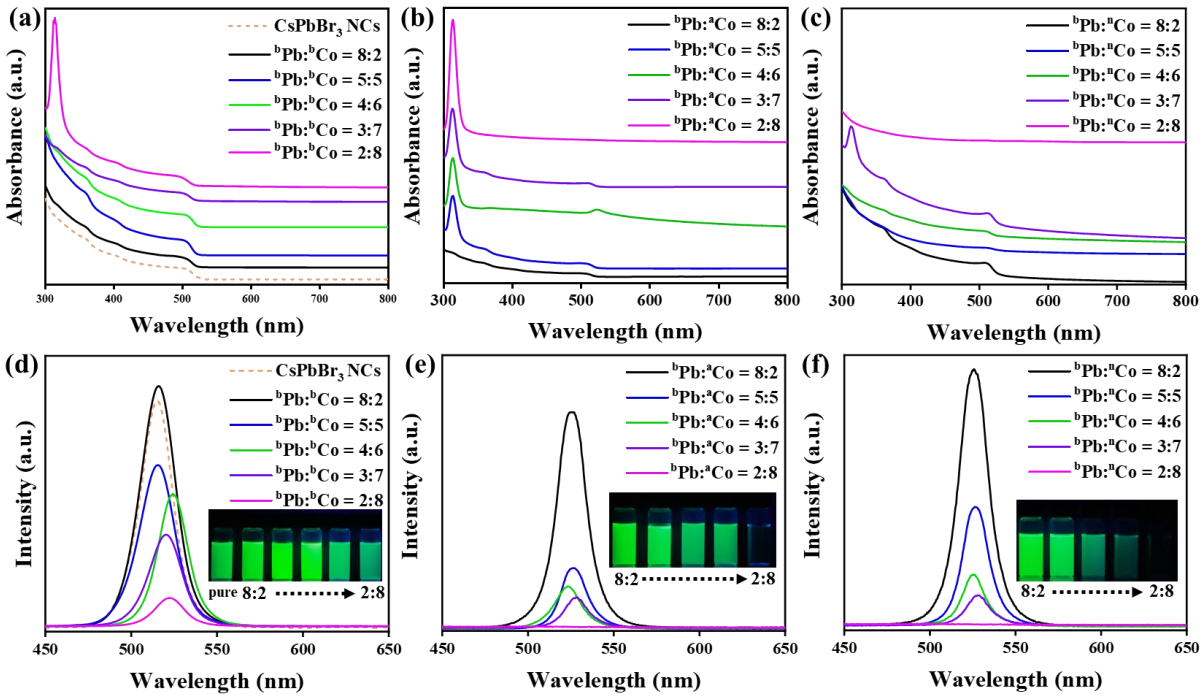

Figure 2. UV–vis absorption spectra of NCs synthesized using different cobalt salts: (a) ^{b}Co, (b) ^{a}Co, (c) ^{n}Co. Corresponding PL spectra with UV-light photographs are shown in (d–f)

The PLQYs of ^{b}Co:CsPbBr$_3$ NCs with precursor ratios of 8:2 and 4:6 were determined to be 60% and 30%, respectively. For ^{a}Co:CsPbBr$_3$ and ^{n}Co:CsPbBr$_3$ NCs (both at 8:2 ratios), the PLQYs were measured as 52% and 78%, respectively. Notably, ^{n}Co:CsPbBr$_3$ NCs exhibited the highest initial PLQY, surpassing that of pure CsPbBr$_3$ NCs (58%). However, these NCs displayed rapid photodegradation, losing emission within minutes, and thus were deemed unsuitable for further investigation. In contrast, ^{b}Co:CsPbBr$_3$ NCs not only demonstrated relatively enhanced PLQY compared to the undoped counterpart but also exhibited improved photostability, making them more promising for subsequent studies.

X-ray diffraction (XRD) measurements were carried out to investigate the crystalline structure of the synthesized Co-doped Cs-Pb-Br NCs. Fig. 3a presents the systematic evolution of XRD patterns for NCs across ^{b}Pb:^{b}Co ratios ranging from 9:1 to 2:8. Diffraction peaks of pure CsPbBr$_3$ and Cs$_4$PbBr$_6$ nanocrystals were compared with those of the synthesized samples. The ^{b}Co: CsPbBr$_3$ NC patterns closely match pristine CsPbBr$_3$ for ratios 9:1 to 3:7. Co-doped CsPbBr$_3$ NCs show diffraction patterns characteristic of CsPbBr$_3$, with orthorhombic distortion evident from peak splitting at 15.21° (expanded spectra in Fig. 3b). Since the ionic radius of Co^{2+} (~0.74 Å) is smaller than that of Pb^{2+} (~1.19 Å), substituting Pb^{2+} with Co^{2+} induces lattice contraction, resulting in a shift of the XRD peaks to higher 2θ values, as shown in Fig. 3b, consistent with TEM confirmed comparable sizes of pure CsPbBr$_3$ and ^{b}Co:CsPbBr$_3$ NCs. Furthermore, as the ^{b}Co feed ratio increases from 3:7 to 2:8, a mixture of orthorhombic CsPbBr$_3$ and Cs$_4$PbBr$_6$ phases emerges, consistent with the absorption spectra that indicate the presence of both phases (Fig. 3a). The appearance of a sharp diffraction peak corresponding to Cs$_4$PbBr$_6$ NCs at the 2:8 ratio suggests the formation of larger crystalline domains. A similar trend in phase evolution is observed with other Co^{2+} precursors, ^{a}Co and ^{n}Co, as shown in Fig. 3c. At lower Co^{2+} concentrations (^{b}Pb:^{a}Co = 8:2; ^{b}Pb:^{n}Co = 8:2), the CsPbBr$_3$ phase predominates, whereas higher doping levels (3:7) result in the formation of Cs$_4$PbBr$_6$ NCs. Transmission electron microscopy (TEM) analysis was employed to confirm morphology and structural changes dependent on the feeding ratios of ^{b}Co, ^{a}Co, and ^{n}Co precursors. In the case of ^{b}Co doping, representative TEM images of ^{b}Co:CsPbBr$_3$ NCs at ^{b}Pb:^{b}Co ratios of 8:2 and 3:7 are shown in Fig. 4a and 4b, respectively. At lower and intermediate ^{b}Co feedings, the cubic morphology of NCs is well preserved, with uniform nanocubes observed. However, at a higher ^{b}Co feeding (2:8), the nanostructures evolve to include both CsPbBr$_3$ nanocubes and larger nanosheets measuring 100–200 nm (Fig. 4c). Additionally, ~100 nm Cs$_4$PbBr$_6$ NCs are present. The larger crystalline domains of these Cs$_4$PbBr$_6$ particles correspond to sharper peaks in the XRD patterns. This observed morphological evolution aligns well with the structural and optical transitions detailed above. With increasing cobalt feeding, the average particle size of the CsPbBr$_3$ NCs grows from 10.76 nm to 18.53 nm, as evidenced by the TEM images and corresponding size distribution histograms shown in Fig. S2. The increase in size is a result of particle growth in the presence of Pb^{2+} deficient conditions. In the case of ^{a}Co fed samples, at a lower cobalt feed ratio (^{b}Pb:^{a}Co = 8:2), the resulting ^{a}Co:CsPbBr$_3$ NCs maintain a well-defined cubic morphology, as shown in Fig. 4d.

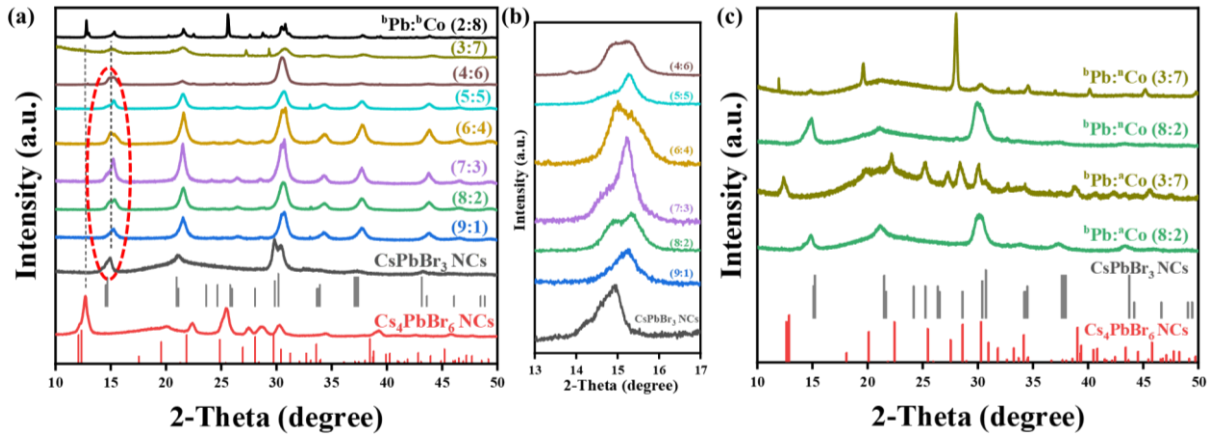

Figure 3. (a) XRD patterns of pure CsPbBr$_3$ and Cs$_4$PbBr$_6$ NCs, along with ^{b}Co:CsPbBr$_3$ NCs and Cs$_4$PbBr$_6$ NCs synthesized with varying ^{b}Pb:^{b}Co ratios (9:1 to 2:8), showing a transition from single-phase CsPbBr$_3$ to mixed-phase CsPbBr$_3$/Cs$_4$PbBr$_6$ at higher Co^{2+} loadings. (b) Magnified view of the region marked in (a), highlighting the peak shifts and splitting near 15.21°. (c) XRD patterns of CsPbBr$_3$ NCs doped with ^{a}Co and ^{n}Co precursors at different concentrations, showing phase evolution from Co:CsPbBr$_3$ to Cs$_4$PbBr$_6$, even at intermediate Co^{2+} loadings

However, at intermediate to high ^{a}Co feeding (^{b}Pb:^{a}Co =3:7 to 2:8), ^{a}Co:CsPbBr$_3$ NCs, the structure changes to a rhombohedral Cs_4PbBr_6 phase (~30 nm), as shown in Fig. 4e and 4f. In contrast, for ^{n}Co feeding, at a lower ratio (^{b}Pb:^{n}Co = 8:2), the ^{n}Co:CsPbBr$_3$ NCs retain a cubic morphology, although with noticeable agglomeration (Fig. 4g). At intermediate ^{n}Co feedings, Cs_4PbBr_6 NCs begin to form, and at higher feedings, irregular and larger-sized Cs_4PbBr_6 structures become dominant, as observed in Fig. 4h and 4i. The effect of cobalt doping in CsPbBr$_3$ nanocubes is evidenced by a noticeable lattice contraction in high-resolution TEM images (Fig. S3), resulting from the substitution of larger Pb^{2+} ions by smaller Co^{2+} ions. This reduction in lattice spacing is consistent with the observed shift of XRD peaks toward higher 2θ values (Fig. 3a). Successful Co^{2+} incorporation into the lattice of CsPbBr$_3$ NCs is further supported by the elemental mapping and scanning transmission electron microscopy (STEM), for different Co^{2+} doping concentrations as well as with various Co^{2+} precursors, as shown in Fig. S4-S14. Quantitative analysis from STEM–EDS reveals doping levels ranging from 0.16 to 3.35 at%, depending on the Co^{2+} feeding ratio. The minimal Co incorporation is also consistent with XPS elemental analysis, where the Pb-to-Co peak ratio is 60:1 for ^{b}Co:CsPbBr$_3$ NCs (8:2). These values are consistent with inductively coupled plasma mass spectrometry (ICP–MS) results, which show Co doping levels of 0.5 and 4.0 at% for ^{b}Pb:^{b}Co ratios of 8:2 and 4:6, respectively. The slightly higher Co content measured by ICP–MS compared to STEM–EDS likely reflects the presence of minor Co-containing species in the supernatant or on the NC surface. Notably, despite the relatively low doping levels, the incorporated Co^{2+} significantly enhances the structural stability of the CsPbBr$_3$ NCs. To understand the side products, the supernatant solution after subjecting the as-synthesized Co-doped CsPbBr$_3$ NCs was washed with methyl acetate and centrifuged at 8000 rpm for 2 min to remove the unreacted precursors and organic ligands. The supernatant solution was used for UV-vis and PL spectral analysis, as shown in Fig. S15. With an increase in the concentrations of Co^{2+} salts, the UV-vis spectra observed a broad absorption peak at 500-700 nm in Fig. S15a-c, which is related to the residual Co^{2+} salts. The supernatant exhibited strong fluorescence at 507 nm and the PL intensity quenched over time due to the presence of excess ligands and metal salts (Fig. S15d-f).

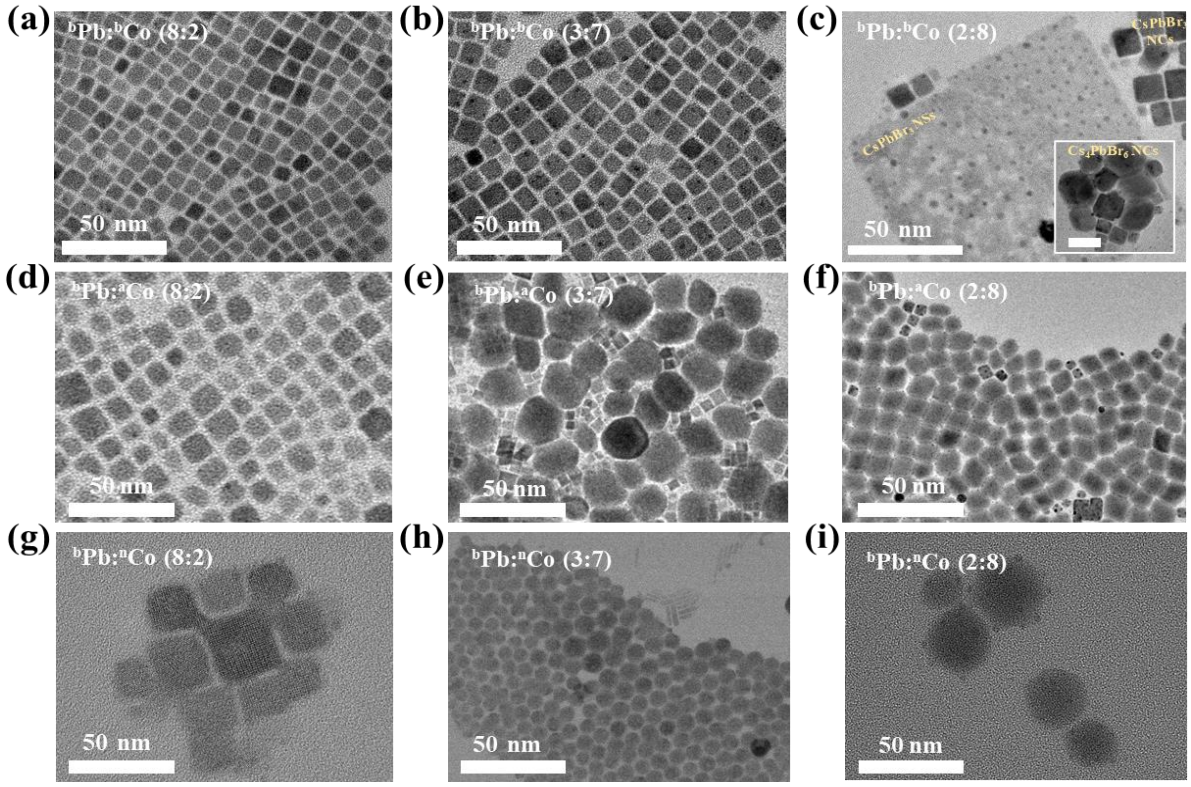

Figure 4. TEM images of Co: CsPbBr$_3$ NCs synthesized using different cobalt precursors (a-c) ^{b}Co, (d-e) ^{a}Co, (g-i) ^{n}Co. The scale bar for the inset of Fig. 4c is 50 nm

1) $2\ CsOA + 3\ PbBr_2 \rightarrow 2\ CsPbBr_3\ NCs + 1\ PbOA_2$
2) $2\ CsOA + 2.4\ PbBr_2 + 0.6\ CoBr_2 \rightarrow 2\ Co_x{:}\ CsPbBr_3 + 0.4\ PbOA + 0.6\ CoOA$ (x= at %)
3) $2\ CsOA + 0.33\ PbBr_2 + 1.33\ CoBr_2 \rightarrow 0.33\ Co_x{:}\ CsPbBr_3\ NCs/NSs + 0.33\ Cs_4PbBr_6 + 1.33\ CoOA_2$
4) $2\ CsOA + 2.4\ PbBr_2 + 0.6\ CoOA \rightarrow 2\ Co_x{:}\ CsPbBr_3 + PbOA$
5) $2\ CsOA + 1.5\ PbBr_2 + 1.5\ CoOA \rightarrow 0.5\ Co_x{:}\ Cs_4PbBr_6 + 1\ PbOA + 1.5\ CoBr_2$ + acetate products
6) $2\ CsOA + 0.3\ PbBr_2 + 1.2\ Co(CH_3COO)_2 \rightarrow 0.5\ Co_x{:}\ Cs_4PbBr_6 + 0.6\ Co(oleate)_2 + 1.2\ CoBr_2$
7) $2\ CsOA + 2.4\ PbBr_2 + 0.6\ Co(NO_3)_2 \rightarrow 2\ Co_x{:}\ CsPbBr_3 + PbOA + 0.6\ CoOA$
8) $2\ CsOA + 0.3\ PbBr_2 + 1.2\ Co(NO_3)_2 \rightarrow$ Decompose to precursor products

As per the previous studies, the necessity of an overstoichiometric Pb^{2+} is required for the formation of $CsPbBr_3$ NCs (eq. 1) [26]. All these experiments were conducted at comparable Cs: Pb and Co: Pb feed ratios, with only the Co precursor anion varied. The results indicate that using Co salts with Br^-, NO_3^-, and CH_3COO^- showed clear differences in optical properties and phase outcomes, confirming that anion identity strongly influences perovskite formation. In addition to the anion effect, the cation also plays a significant role. Two major factors, such as replacing Pb^{2+} ions with Co^{2+} ions and the role of anions, whose effects are discussed below and presented by representative equations 2 to 8. Systematic variation of the Pb:Co feeding ratio across $CoBr_2$, $Co(OAc)_2$, and $Co(NO_3)_2$ revealed that the coordinating anion plays a pivotal role in modulating precursor reactivity and Pb^{2+} availability. In the case of $CoBr_2$, excess Br^- contributes weakly to Pb^{2+} complexation, preserving rapid monomer release and enabling the formation of $CsPbBr_3$ NCs or nanosheets even at high ^{b}Co loading [27]. With increasing ^{b}Co loading, a significant reduction in Pb content was observed, which in turn led to a relative excess of Cs^+ ions. This compositional imbalance suppressed the formation of Br-bridged $[PbBr_6]^{4-}$ octahedra, favoring instead the formation of isolated octahedra characteristic of the Cs_4PbBr_6 structure [28].

To validate this hypothesis, we conducted control reactions using varying Cs: Pb feeding ratios in the absence of cobalt salts (Fig. S16). At a Cs: Pb ratio of 1:2, $CsPbBr_3$ NCs were predominantly formed. However, reducing the Pb content by half resulted in the emergence of Cs_4PbBr_6 as the dominant phase (Fig. S16). These observations indicate that, independent of $CoBr_2$ concentration, a deficiency in Pb and Br favors the formation of Cs_4PbBr_6. By contrast, $Co(OAc)_2$ introduces strongly chelating acetate ligands that sequester Pb^{2+} into stable complexes, effectively reducing free Pb^{2+} concentrations and favoring the formation of the Cs-rich Cs_4PbBr_6 phase [29]. This effect is further amplified by acetate-induced shifts in local pH, which enhance oleate coordination and suppress Pb^{2+} reactivity. Notably, $Co(NO_3)_2$ destabilizes the reaction entirely, likely due to the oxidative character of nitrate disrupting ligand integrity and perovskite nucleation. These results suggest that the ligand field strength and complexation dynamics of the cobalt precursor critically govern the effective Cs: Pb ratio and thereby direct the structural outcome of the final product. X-ray photoelectron spectroscopy (XPS) was employed to analyze the surface chemical composition and electronic states of $^{b,\,n,\,a}$Co: $CsPbBr_3$ NCs (Fig. S17 and S18). As shown in Fig. S17, the survey spectrum showed all the elements present in the Co-doped halide perovskites. The spectra were standardized by the C 1s peak at 284.8 eV, indicating that the $^{b,\,n,\,a}$Co: $CsPbBr_3$ NCs contain Cs, Pb, Br, and Co elements. The high-resolution XPS spectra of the individual elements are shown in Fig. 5. As shown in Fig. 5a, the $^{b,\,n,\,a}$Co: $CsPbBr_3$ NCs exhibited stable Cs 3d binding energy as Co^{2+} replaced the Pb^{2+} site, with little influence on the Cs site. In Fig. 5b, the Pb $4f_{7/2}$ and Pb $4f_{5/2}$ peaks appear at 137.91 eV and 142.78 eV, respectively. For the ^{b}Co:$CsPbBr_3$ NCs (8:2), the Pb 4f binding energy exhibits a slight positive shift of 0.2 eV compared to pristine $CsPbBr_3$ NCs. The increasing binding energies indicate that Co doping induced lattice contraction leads to strengthening the bonding between Pb-Br. With increasing feed ratio, ^{b}Co:$CsPbBr_3$ NCs (3:7) also show a slightly higher Pb 4f binding energy with peak broadening. The peak broadening indicates mixed morphologies, consistent with TEM observations, suggesting that higher feed ratios promote nanosheet formation. In the case of ^{a,n}Co:$CsPbBr_3$ NCs (8:2), the peak positions show a very slight positive shift, indicating only marginal Co doping in these systems. However, in other cases, such as ^{a}Co:$CsPbBr_3$ NCs (3:7) and ^{n}Co:$CsPbBr_3$ NCs (3:7), the Pb 6f peaks consistently shift toward higher binding energy (Fig. 5b). A higher binding energy shift of 0.6-0.7 eV compared to pristine $CsPbBr_3$ NCs, indicating the formation of Cs_4PbBr_6. This shift can be attributed to the phase transformation from $CsPbBr_3$ to Cs_4PbBr_6. Where Pb experiences a more localized and ionic environment with reduced electronic screening.

The Br $3d_{5/2}$ and $3d_{3/2}$ binding energies, observed at 69.07 eV and 68.01 eV, respectively, and their shifts upon Co-doping are shown in Fig. 5c. For ^{b,a,n}Co:$CsPbBr_3$ NCs (8:2) and ^{b}Co:$CsPbBr_3$ NCs (3:7), the Br 3d peaks shift toward higher binding energies, indicating a slight Pb–Br lattice contraction due to partial substitution of Pb^{2+} with Co^{2+}, while the perovskite structure remains intact. In contrast, ^{a,n}Co:$CsPbBr_3$ NCs (3:7) exhibit Br 3d shifts to lower binding energies, consistent with increased Cs_4PbBr_6 formation. This phase evolution weakens Pb–Br interactions and perturbs the Br electronic environment, highlighting the combined effects of excessive Co incorporation and anion identity on lattice structure [17]. This is attributed to the fact that Co^{2+} replaced Pb^{2+} and influenced the interaction between Pb-Br, promoting the formation of the Co-Br bond and changing the chemical environment, causing the lattice contraction. Fig. 5d shows the Co 2p binding energy with a Co $2p_{3/2}$ broadened peak with three peaks at 780.69 eV (for Co^{2+}), 782.93 eV (for Co^{3+}) and a satellite peak at 785.64 eV and a Co $2p_{1/2}$ broadened peak with two peaks at 793.28 eV (for Co^{2+}) and 795.32 eV (for Co^{3+}). The weak intensities of Co peaks across all samples are consistent with a low level of Co incorporation. Notably, the relative contributions of Co^{2+} and Co^{3+} vary with precursor identity and feed ratio, indicating that the oxidation environment and coordination geometry of cobalt are sensitive to synthetic conditions.

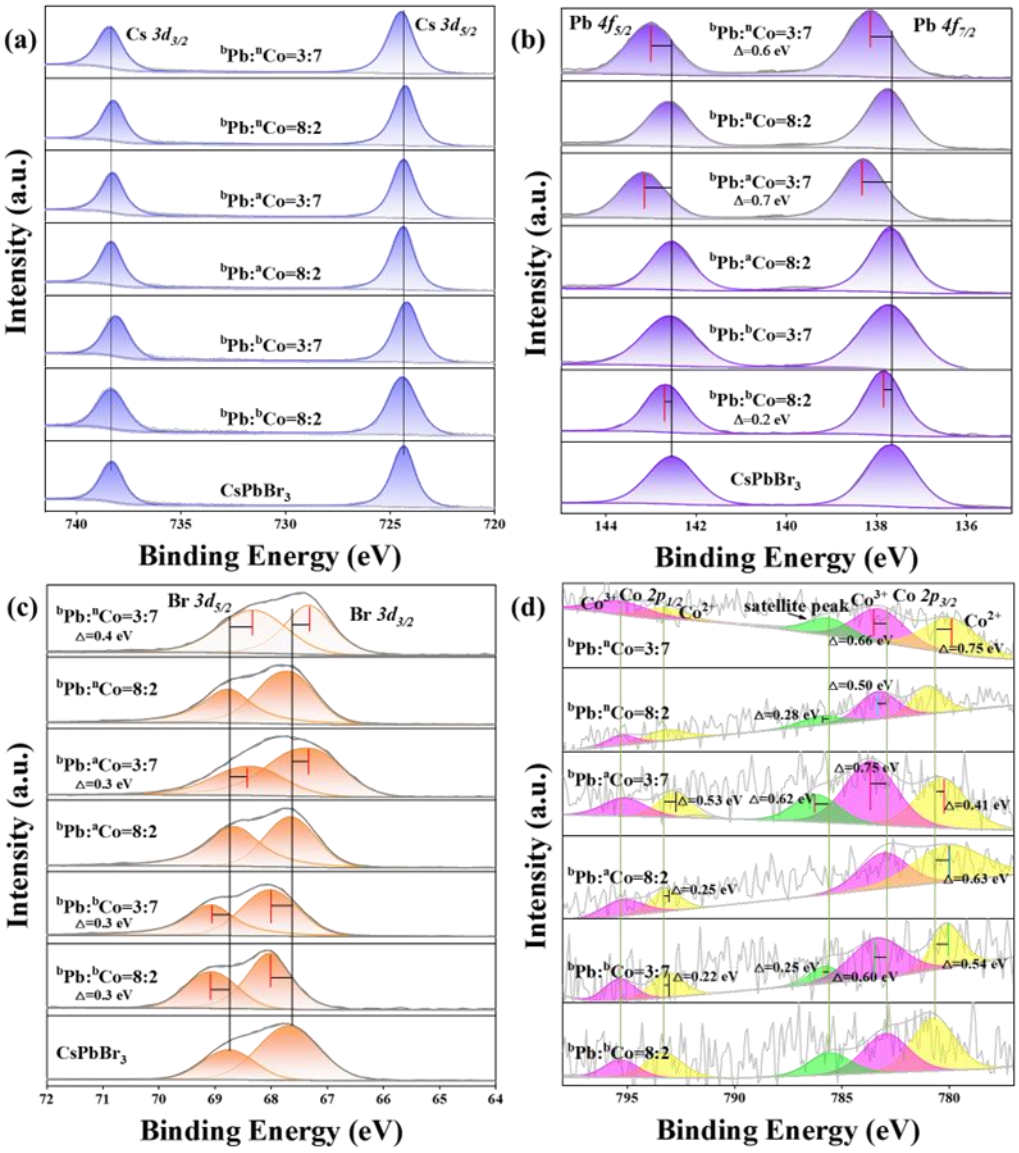

Figure 5. High-resolution XPS spectra corresponding to Cs 3d (a), Pb 4f (b), Br 3d (c) and Co 2p (d) with different types of cobalt salts doped into Cs-Pb-Br NCs

Collectively, the XPS data confirm the successful incorporation of cobalt into the $CsPbBr_3$ lattice and reveal that higher ^{n,a}Co feeding concentrations promote phase segregation toward Cs_4PbBr_6.

To understand the impact of Co^{2+} and defect passivation on $CsPbBr_3$ NCs, we employed femtosecond pump-probe transient absorption (fs-TA) spectroscopy on both $CsPbBr_3$ NCs and ^{b}Co:$CsPbBr_3$ NCs (8:2). Both samples were excited with a 365 nm pump beam, and the resulting spectral evolution was monitored at different time delays using a broadband white-light supercontinuum probe beam. Fig. 6a and 6b exhibit the fs-TA map of $CsPbBr_3$ NCs and ^{b}Co:$CsPbBr_3$ NCs (8:2), respectively. Upon photoexcitation, these two samples both display a pronounced ground-state bleach (GSB) at 495 nm due to the state-filling effect and photo-induced absorption (PIA) on either side of the bleach signal [30, 31]. Fig. 6c and 6d show a rapid decay of the GSB at 495 nm after 1 ns for $CsPbBr_3$ NCs and ^{b}Co:$CsPbBr_3$ NCs (8:2), respectively. Further, the exciton recovery kinetics were plotted in bleach maxima position (495 nm) to understand the influence of Co^{2+} and defect passivation on $CsPbBr_3$ NCs (Fig. 6e). The ^{b}Co:$CsPbBr_3$ NCs (8:2) exhibit slower carrier relaxation dynamics than those of undoped samples, which is ascribed to the Co^{2+} doping and Br^- passivation, which enhanced the radiative recombination process of electrons and holes. Hence, $CoBr_2$ efficiently eliminates the V_{Br} defects and weakens the defect-mediated (nonradiative) recombination pathway, which may benefit the subsequent optoelectronic applications [31-33]. Time-resolved photoluminescence (TRPL) measurements of ^{b}Co:$CsPbBr_3$ NCs (8:2) and pristine $CsPbBr_3$ NCs are shown in Fig. 6f and summarized in Table S1. Pristine $CsPbBr_3$ NCs exhibit a dominant fast decay component (τ_1 = 0.4 ns, A_1 = 0.8) attributed to defect-assisted nonradiative recombination, while a slower radiative channel (τ_2 = 3.5 ns, A_2 = 0.2) contributes modestly, giving an average lifetime (τ_{avg}) of 2.53 ns. For ^{b}Co:$CsPbBr_3$ NCs (8:2), the fast decay (τ_1 = 0.4 ns, A_1 = 0.7) remains prominent, but the radiative channel is prolonged (τ_2 = 4.5 ns, A_2 = 0.3), extending τ_{avg} to 3.8 ns.Similar behavior is observed for the 5:5 sample (τ_{avg}=3.9 ns), whereas excessive Co incorporation (4:6) drastically reduces τ_{avg} to 1.0 ns, consistent with the generation of additional trap states that accelerate nonradiative recombination (Fig S19a). At the optimal Pb: Co ratio of 8:2, the longer lifetime reflects suppressed nonradiative pathways through effective defect passivation, correlating with enhanced PLQY. In contrast, over-doping (4:6) promotes trapping in non-emissive states, leading to quenching centers. This passivation-to-trapping transition explains the non-monotonic luminescence behavior with increasing Co content.

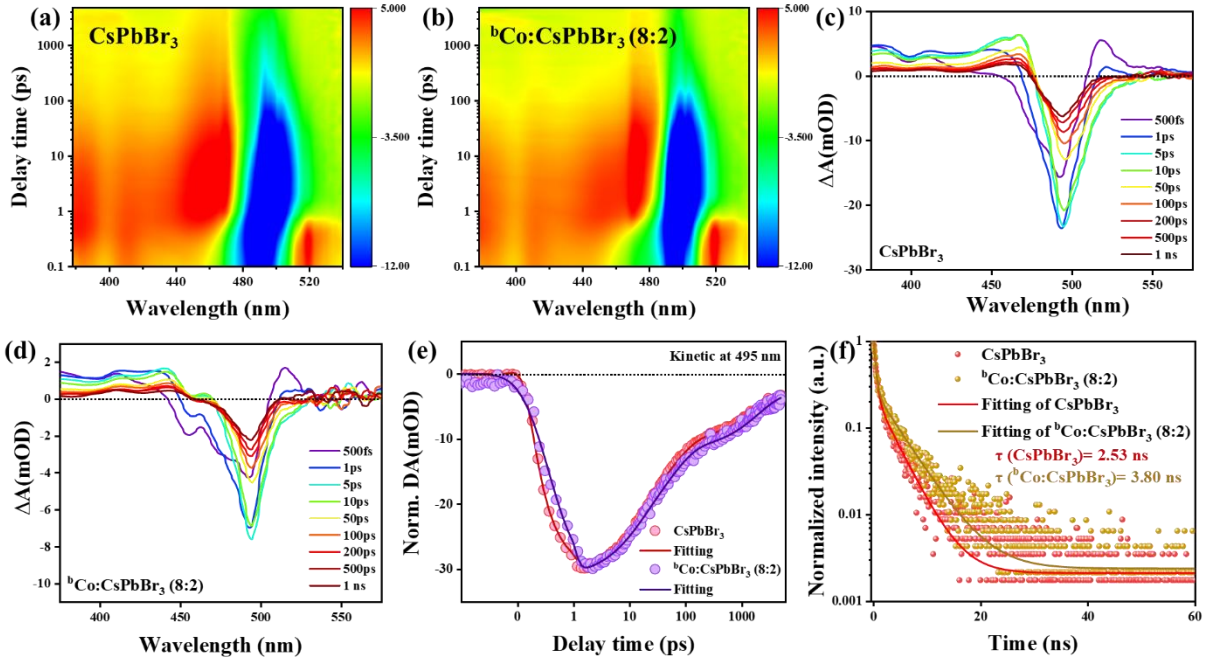

Figure 6. fs-TA map of (a) $CsPbBr_3$ NCs, (b) ^{b}Co:$CsPbBr_3$ NCs (8:2). TA spectra of (c) $CsPbBr_3$ NCs, (d) ^{b}Co:$CsPbBr_3$ NCs (8:2) at selected time delays. (e) TA kinetic traces and exponential fitting at 495 nm of pristine $CsPbBr_3$ and ^{b}Co:$CsPbBr_3$ NCs (8:2). (f) TRPL measurement of pristine $CsPbBr_3$ and ^{b}Co:$CsPbBr_3$ NCs (8:2)

Notably, ^{a}Co:CsPbBr$_3$ (8:2) and ^{n}Co:CsPbBr$_3$ (8:2) NCs display τ_{avg} values of 1.7 ns and 4.3 ns, respectively, which align with their PLQY trends: acetate ligands yield poor passivation and trap-dominated emission, while nitrate favors more efficient radiative decay but suffers from poor stability (Fig S19b). Although ^{b}Co:CsPbBr$_3$ NCs (8:2) achieve enhanced PLQY and prolonged radiative lifetimes, their stability remains inferior compared to the other systems. In order to understand the role of doping in CsPbBr$_3$ on the band gap, we performed density functional theory (DFT) with a plane-wave pseudopotential approach (details in the methods section); their unit cells are presented in Fig. 7a and b. The electronic structure analysis reveals that Co doping in CsPbBr$_3$ significantly modifies the band gap, introducing mid-gap states that enhance electronic conductivity. Projected and total density of states (PDOS/TDOS) indicate strong hybridization between Co-3d and Br-4p orbitals, suggesting increased carrier mobility and altered optical transitions. These modifications imply that Co-doped CsPbBr$_3$ could exhibit tunable electronic and optoelectronic behavior. Fig. 7 presents the computed electronic band structures alongside the TPDOS and TDOS (PDOS/TDOS) for pristine CsPbBr$_3$ and its Co^{2+}-doped derivatives, highlighting the impact of doping on the electronic responses.

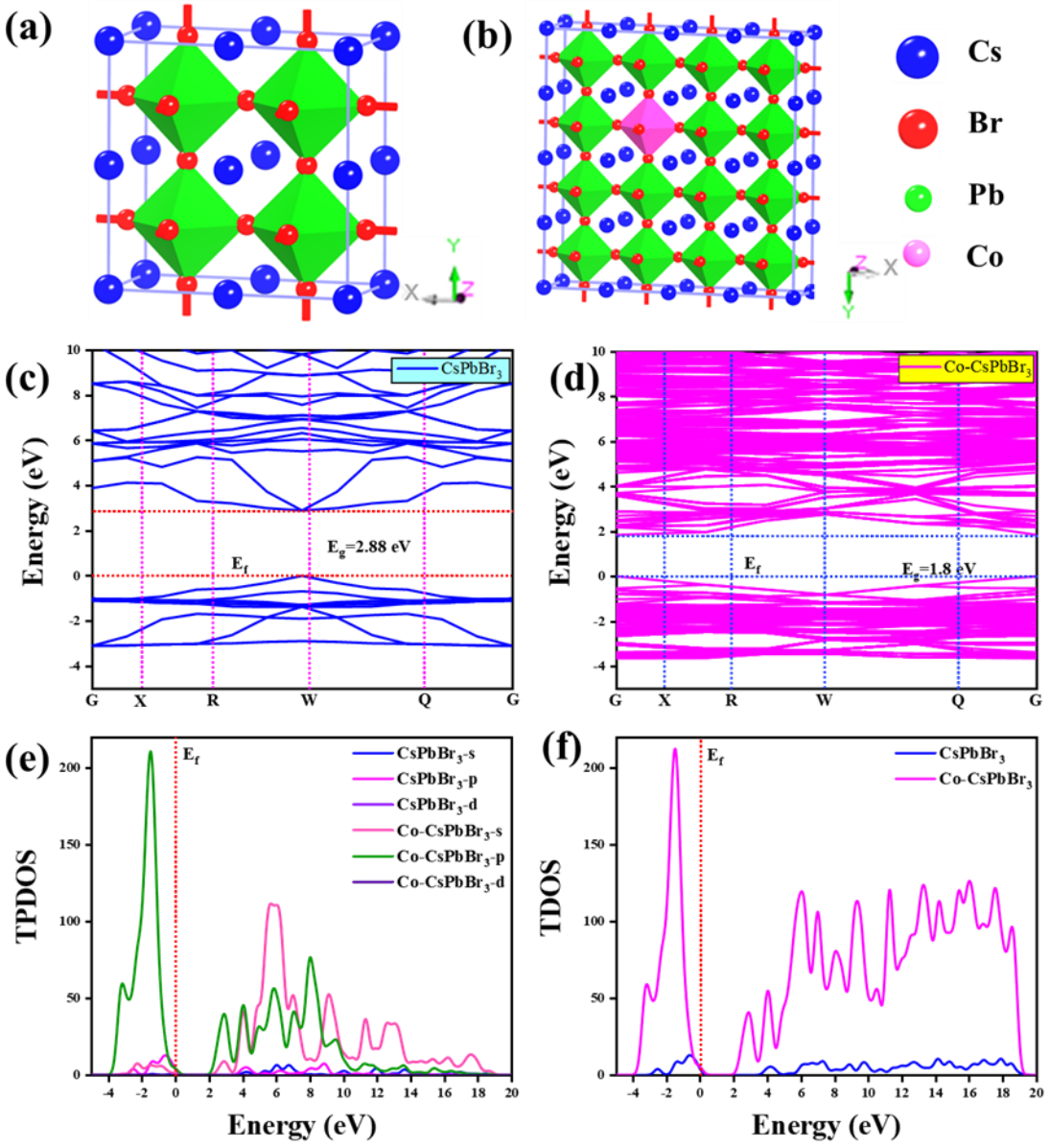

Figure 7. Schematic representation of pristine (a) and Co-doped (b) CsPbBr$_3$ NCs. Computed electronic band gaps and density of states for CsPbBr$_3$ before and after Co doping: (c) Band structure of pristine CsPbBr$_3$, (d) Band structure of Co-doped, (e) TPDOS and (f) TDOS for pristine and doped systems

Fig. 7c and 7d illustrate the computed electronic band structures of pristine and Co-doped perovskites, mapped along the high-symmetry directions of the first Brillouin zone (FBZ). The selected k-path, G–X–R–W–Q-G, corresponds to the $Pm\bar{3}m$ space group for both systems, enabling a detailed comparison of their electronic behavior. The pristine $CsPbBr_3$ exhibits a direct band gap of 2.88 eV, in strong agreement with the experimental value of ~2.55 eV [24]. Upon Co^{2+} incorporation, the band gap decreases significantly to 1.8 eV, reflecting the influence of transition metal doping on the electronic structure. Both pristine and Co-doped perovskites retain direct band gap characteristics; however, notable shifts in the conduction band minimum (CBM) and valence band maximum (VBM) are observed. In the pristine system, the CBM and VBM are located at the W point, whereas Co^{2+} substitution induces an upward shift of the CBM, attributed to enhanced free carrier density and a redistribution of states near the Fermi level. While the overall topology of the band structure remains consistent, subtle variations in the band gap arise from atomic size mismatch between Pb and Co, as well as hybridization effects involving Co-3p, Pb-5p, and Br-4p orbitals, demonstrating the tunability of electronic properties through controlled Co doping. Fig. 7e and 7f present the computed total projected density of states (TPDOS) and total density of states (TDOS) for pristine and Co^{2+}-doped $CsPbBr_3$ systems. These analyses reveal the state's contributions shaping the valence and conduction bands and highlight the electronic modifications induced by Co^{2+} incorporation. In the pristine $CsPbBr_3$, the valence band is primarily composed of Br-4p and Pb-6s states, while the conduction band is dominated by Pb-6p states weakly hybridized with Br-4p orbitals, with minimal contributions from Cs^{1+} orbitals. Upon Co^{2+} doping, a pronounced increase in the electronic density near the valence band maximum is observed, reflecting additional states introduced by Co-3d orbitals. Notably, the TDOS shows a significant peak shift towards the Fermi level, indicating enhanced carrier density and potential improvement in electronic conductivity. Total TDOS analysis confirms that while the overall band structure topology remains consistent, hybridization between Co-3d, Pb-6p, and Br-4p states modulates the band edges, resulting in a narrowed band gap and enhanced valence band density. These findings demonstrate that Co^{2+} doping effectively tunes the electronic structure of $CsPbBr_3$, providing a pathway for improved optoelectronic performance. The stability of $^{b,a,n}Co:CsPbBr_3$ NCs ($^{b}Co:CsPbBr_3$ at 8:2 and 5:5; $^{a,n}Co:CsPbBr_3$ at 8:2) and pristine $CsPbBr_3$ NCs was systematically evaluated under multiple conditions, including solution stability at room temperature (RT) and 50 °C, UV light exposure, and solid-state stability at 80 °C (Figs. S20-28). For solution-phase studies, the NCs were dispersed in hexane (10 µL/mL), and their temporal stability was monitored via absorption and PL spectroscopy over one week at RT and 20 h at 50 °C. Among all samples, $^{b}Co:CsPbBr_3$ NCs (8:2) exhibited outstanding RT stability, showing negligible changes in both absorption (Fig. S20b) and PL positions (Fig. S21b), whereas $^{b}Co:CsPbBr_3$ NCs (5:5) showed only a minor reduction in PL intensity (Figs. S20c and S21c). TEM analysis confirmed that the morphology and particle size of $^{b}Co:CsPbBr_3$ NCs (8:2 and 5:5) remained intact (Fig. S22). In contrast, pristine $CsPbBr_3$ NCs displayed a blue shift in absorption and PL, indicative of particle size reduction (Figs. S20a and S21a). The $^{a}Co:CsPbBr_3$ NCs showed a relative blue shift in PL over two days, reflecting lower stability compared to pristine $CsPbBr_3$, which was corroborated by absorption measurements and TEM imaging that revealed increased polydispersity and reduced particle size (Figs. S20d, S21d, and S22). The $^{n}Co:CsPbBr_3$ NCs degraded rapidly, with pronounced absorption changes and PL quenching within one day, while TEM confirmed particle disintegration, likely due to the reactive nature of nitrate ions with the perovskite lattice (Figs. S20e, S21e, and S22). XRD analysis further supported these observations (Fig. S27): $^{b,a}Co$-doped $CsPbBr_3$ NCs retained the orthorhombic perovskite phase over several weeks, whereas $^{b}Co:CsPbBr_3$ NCs (5:5) partially transformed into a Cs_4PbBr_6-perovskite mixed phase, and $^{n}Co:CsPbBr_3$ NCs lost characteristic perovskite diffraction peaks upon ageing. Collectively, the stability trend follows: $^{b}Co:CsPbBr_3$ NCs > pristine $CsPbBr_3$ NCs > $^{a}Co:CsPbBr_3$ NCs > $^{n}Co:CsPbBr_3$ NCs. This stability trend persisted at elevated temperatures (50 °C, 20 h), with $^{b}Co:CsPbBr_3$ NCs (8:2) remaining the most stable among all samples (Fig. S28). Meanwhile, the photostability of the NCs was assessed under UV illumination (Figs. S23-S25). For $^{b,a}Co:CsPbBr_3$ NCs (8:2), XRD patterns remained stable (Fig. S27), with increased peak sharpness indicative of particle growth, consistent with the scattering component observed in absorption and the red shift in PL positions. TEM analysis confirmed this increase in particle size after UV exposure. In contrast, $^{b}Co:CsPbBr_3$ NCs (5:5) underwent structural changes, partially transforming from $CsPbBr_3$ to Cs_4PbBr_6. $^{n}Co:CsPbBr_3$ NCs (8:2) decomposed rapidly under

illumination, with UV–vis and PL spectra showing substantial loss of characteristic $CsPbBr_3$ features. In all cases, significant PL quenching and a rise of the scattering component in absorption spectra were observed. The overall photostability follows the order: ^{b}Co:$CsPbBr_3$ NCs > pristine $CsPbBr_3$ NCs > ^{a}Co:$CsPbBr_3$ NCs > ^{n}Co:$CsPbBr_3$ NCs, confirming the superior stability of ^{b}Co:$CsPbBr_3$ (8:2) relative to ^{a,n}Co:doped analogues.

Fourier transform infrared (FTIR) spectra of all five samples, recorded before and after UV exposure, showed minimal changes, indicating that the overall chemical structure of the NCs remained largely intact (Fig. S26). In parallel, solid-state, temperature-dependent PL measurements were performed at 80 °C over several hours (Fig. S28b). Among ^{b}Co:$CsPbBr_3$ (8:2) exhibited superior stability compared to ^{a,n}Co-doped NCs, although a slight PL quenching was observed relative to pristine $CsPbBr_3$ NCs. This minor decrease in emission can be attributed to enhanced ion migration induced by Co^{2+} incorporation, where both cationic and anionic species become more mobile under thermal stress, slightly reducing PL efficiency. Importantly, this modest quenching does not compromise the structural integrity or device-relevant stability of the NCs, highlighting the distinct effects of Co^{2+} doping in solution versus the solid state. Perovskite NCs are promising light-emitting materials, with stability significantly enhanced by surface passivation that reduces defects and non-radiative losses [34-37].

The improved stability observed in ^{b}Co:$CsPbBr_3$ NCs prompted a comparative evaluation of their performance against both undoped $CsPbBr_3$ NCs and other Co-doped variants. To evaluate the practical application of Co-doped $CsPbBr_3$ NCs, white LEDs were fabricated by combining the solid states of Co-doped $CsPbBr_3$ NCs and commercial red powder (K_2SiF_6:Mn^{4+}) with a blue LED. The result of the PL spectrum of the WLED device is shown in Fig. 8. The PL spectrum is composed of five emission peaks belonging to the blue LED chip (455 nm), sample phosphor (near 530 nm) and commercial red powder (612 nm, 630 nm and 646 nm), respectively. Fig. 8a-8e shows changes in PL intensity observed under different currents ranging from 20 mA to 320 mA for different Co^{2+} doped $CsPbBr_3$ NCs.

With the increase of device current, the emission intensity of Co^{2+} doped $CsPbBr_3$ NCs showed an increasing trend with a gradual rise in current. However, when the operating current reached 320 mA, the CIE color coordinates shifted significantly from initial white light to purplish-pink luminescence region for $CsPbBr_3$ NCs in Fig. 8f, ^{b}Pb: ^{b}Co = 8:2 in Fig. 8g, and ^{b}Pb:^{b}Co = 5:5 in Fig. 8h, blue luminescence region for ^{b}Pb:^{n}Co = 8:2 in Fig. 8i, and ^{b}Pb:^{a}Co = 8:2 in Fig.8j, due to the electrical quenching of the green light components ($CsPbBr_3$ NCs). The values of the luminous efficacy of each sample are 25.81, 14.04, 27.7, 2.54, and 1.05 lm/W at 20 mA, respectively. The specific values under different currents are listed in Table S2, and the changes in luminous efficacy of each sample under different currents are shown in Fig. S29. $CsPbBr_3$ has low thermal conductivity (~0.5 $W \cdot m^{-1} \cdot K^{-1}$) [38], so at high driving currents (320 mA), joule heating can raise the emissive layer temperature to 80–120 °C. Solid-state PL measurements reveal emission quenching, while the ligands remain intact, indicating that lattice expansion and thermal stress rather than ligand desorption are the dominant factors.

We also evaluated the Rf, which refers to a metric used to evaluate the color fidelity or color accuracy of a display device, was also evaluated. A high Rf value (IES TM-30 fidelity index) indicates that the display is reliable for color-critical tasks. Among the 5 WLEDs, the highest fidelity index Rf value of 67 (at 20 mA) corresponds to ^{b}Pb:^{n}Co = 8:2 doped $CsPbBr_3$ NCs.

However, this ^{b}Pb:^{n}Co = 8:2 doped $CsPbBr_3$ NCs undergoes structural distortion upon the increase in the current; hence, it is not considered ideal in terms of its Rf beyond 240 mA (Fig. 8i, orange arrow). Similar trends were also observed in the case of pristine $CsPbBr_3$ NCs (specific values are shown in Table S3). All samples Rf changes under different currents are shown in Fig. 8k, ^{b}Pb:^{b}Co = 8:2, ^{b}Pb:^{b}Co = 5:5, and ^{b}Pb:^{a}Co = 8:2 show relatively stable Rf values with the current changes; these indicate Co^{2+} doping can increase the device stability. The constructed WLED device for ^{b}Pb:^{b}Co =8:2 doped $CsPbBr_3$ NCs exhibited the CIE color coordinates (0.301,0.342) (Fig. 8g), a color temperature of 7024 K. The obtained color gamut of the assembled lighting display is compared with the NTSC and Rec. 2020 standards (Fig. 8l).

This work's color gamut can cover about 122.9 % and 91.7 % of the NTSC and Rec. 2020, respectively (The values for each sample are shown in Table S4). The WLED device photographs with unlit and lit under current are shown in Fig. 8m and 8n, respectively. The color rendering index (Ra) serves as another critical parameter (CIE standard) for evaluating these five WLEDs. A higher Ra value indicates that the emitted light more closely approximates the true color of materials.

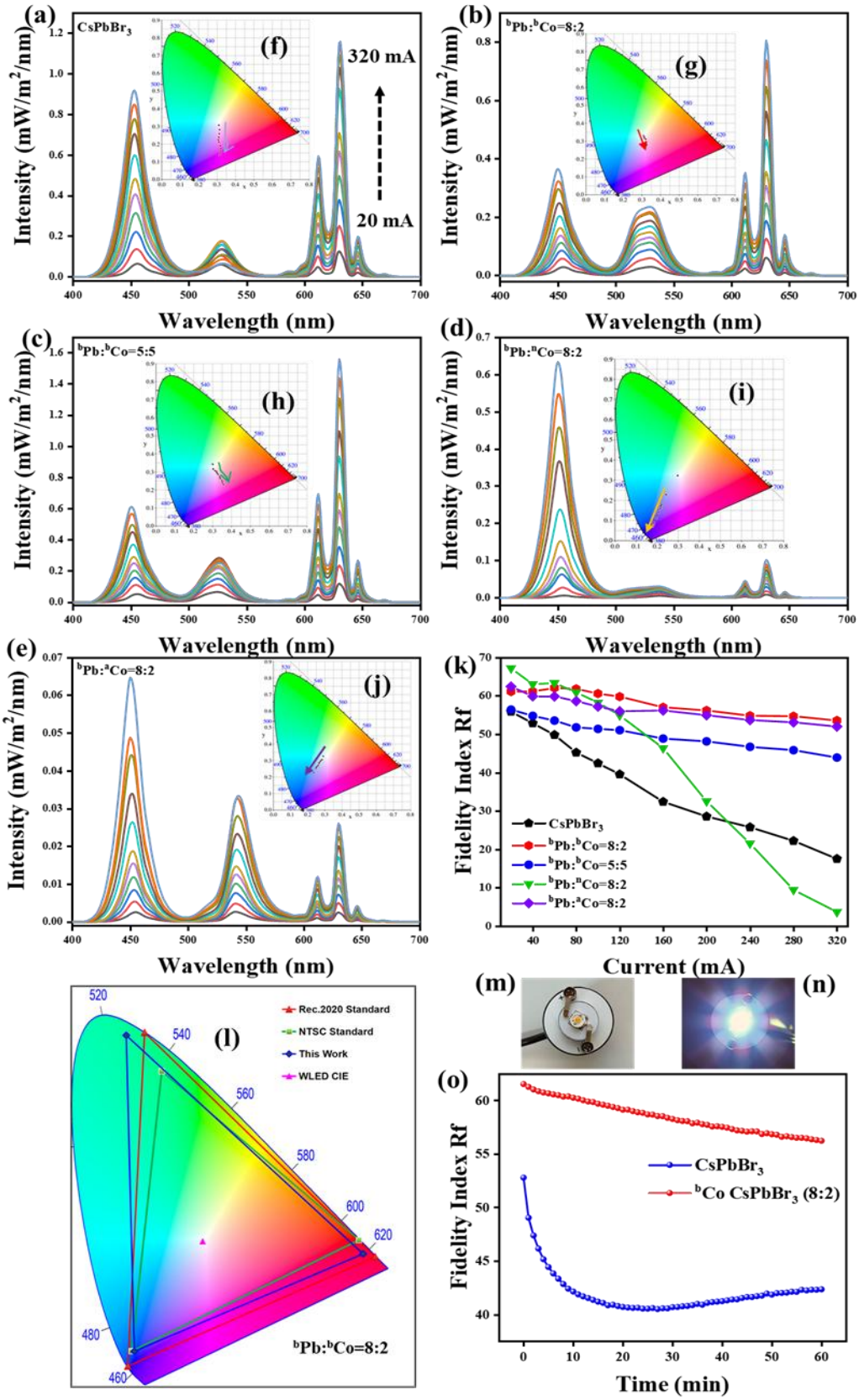

Figure 8. PL spectra of WLEDs under different currents (from 20 mA to 320 mA). (a) $CsPbBr_3$, (b) $^{b}Pb:^{b}Co=8:2$, (c) $^{b}Pb:^{b}Co$ = 5:5, (d) $^{b}Pb:^{n}Co=8:2$, and (e) $^{b}Pb:^{a}Co$ =8:2 (f)-(j) are the corresponding changes of CIE color coordinates of the WLED device under different currents (marked with arrows). (k) Changes of fidelity index Rf with different NCs under different currents. (l) Comparison of the color gamut of WLED with the NTSC Television Standard and the Rec. 2020 Standard for $^{b}Pb:^{b}Co=8:2$. The CIE color coordinates of the WLED device are at (0.31, 0.33). (m) and (n) display $^{b}Pb:^{b}Co=8:2$ related photographs of the device and the working WLEDs. (o) Comparison of the performance of $CsPbBr_3$ and ^{b}Co-$CsPbBr_3$ (8:2) WLEDs at 20 mA over 1 hour

Tables S5-S9 present the variations in Ra value of these WLEDs fabricated using pure $CsPbBr_3$ and different Co^{2+} doped $CsPbBr_3$ NCs under varying currents. Among all Co-doped samples, the ^{a,b}Co:$CsPbBr_3$ (8:2) exhibits the highest Ra value and optimal stability. Notably, all Co-doped WLEDs demonstrate higher Ra values compared to the pure $CsPbBr_3$-based device.

To evaluate the long-term stability of WLED fabricated using Co-doped $CsPbBr_3$, we compared the performance of WLEDs based on pristine $CsPbBr_3$ and ^{b}Co:$CsPbBr_3$ (8:2) under 20 mA over 1 hour. The results reveal that the PL intensity decreases over time for both devices; however, the ^{b}Co-doped $CsPbBr_3$-based WLED exhibits relatively higher stability compared to the pristine $CsPbBr_3$. For ^{b}Co:$CsPbBr_3$ (8:2), ~92% of the initial intensity was retained (65 → 60) after 10 min, and ~88% (65 → 57) after 1 h.

In contrast, undoped $CsPbBr_3$ retained only ~78% of its initial intensity (52 → 40) within 10 min (Fig. 8o). Fig. S30 presents the changes in PL intensity of these two WLEDs during the 1-hour testing at 20 mA. In the CIE standard, detailed results on the Ra values of $CsPbBr_3$ NCs and ^{b}Co-doped $CsPbBr_3$-based WLEDs under 20 mA during prolonged testing are listed in Tables S10 and S11, respectively. The Ra of the pristine $CsPbBr_3$-based WLED drops drastically from 42 to 5, retaining only ~12% of its initial value, which underscores the device's poor ability to reproduce true colors. In contrast, the ^{b}Co-doped $CsPbBr_3$-based WLED exhibits a much smaller decrease, from 56 to 47, thereby preserving ~84% of its initial Ra. This markedly improved retention demonstrates the superior stability of the ^{b}Co-doped $CsPbBr_3$ NCs, highlighting their potential for achieving more reliable color quality in WLED applications.

4. Conclusions

This study elucidates the role of counter anions in the dopant precursor and the concentration of cobalt ions critically influence the structural, optical, and electronic behavior of Co^{2+}-doped $CsPbBr_3$ NCs synthesized via hot-injection. By comparing $CoBr_2$ (^{b}Co), $Co(NO_3)_2$ (^{n}Co), and $Co(CH_3COO)_2$ (^{a}Co) as dopant sources, we reveal that the dopant's counterion plays a central role in governing phase stability and luminescence characteristics.

Among the three, ^{b}Co emerged as the optimal precursor, offering a favorable trade-off between photoluminescence intensity (~60% retention) and structural integrity of the optically active orthorhombic perovskite phase. In contrast, ^{n}Co precursors yielded higher initial PL (~80%) but introduced quick instability, promoting partial or full transformation to Cs_4PbBr_6. Notably, excessive Co^{2+} doping (e.g., $PbBr_2$:^{b}Co = 2:8) triggered phase segregation and morphological changes, diminishing emissive performance.

In device integration, ^{b}Co:$CsPbBr_3$ NCs (8:2) enabled white LEDs with consistent emission across 20–320 mA and achieved 122.9% NTSC and 91.7% Rec. 2020 color coverage. Importantly, ^{b}Co:$CsPbBr_3$ retained ~92% of its initial color fidelity over the period of 10 minutes, whereas pristine $CsPbBr_3$ retained only ~78%. The results suggest the ^{b}Co:$CsPbBr_3$ NCs demonstrated high color accuracy, superior stability compared to their counterparts. Collectively, this work underscores the importance of dopant–ligand chemistry in tuning perovskite NCs, offering new design principles for achieving both stability and functionality in optoelectronic applications.

Associated Content

Supporting Information: Synthesis and device fabrication procedures and characterization of perovskite NCs are available.

Authors Contribution

U.T. conceived the idea and supervised the research. H.Z., R.H., and A.S. performed synthesis, optical, and morphological characterizations of the perovskites. C.W., A.N., and J.B. perform TRPL and TA measurements. Y.W. and M.P. guided the experiments and writing. S.K., M.Me, N.P. and M.M. interpreted the results of characterization. U.T. and H.Z. wrote the paper. All authors have discussed the content and contributed to the manuscript.

Declaration of competing interest

The authors declare no competing financial interest.

Acknowledgments

Thanks are due to the National Natural Science Foundation of China (NSFC Grant 22050410280) and Chengdu Science and Technology Bureau (Grant 2022YFWZ0004). We would like to acknowledge the University of Electronic Science and Technology of China (UESTC) for their steadfast support of the graduate studies. We thank the State Key Laboratory of Electronic Thin Films and Integrated Devices at the UESTC for the support.

Ethics Approval

The experimental protocol underwent thorough evaluation and received formal approval from the Laboratory Animal Ethics Committee at Tabriz University of Medical Sciences, Tabriz, Iran, under Approval No. IR.TBZMED.AEC.1402.118. This approval confirms adherence to ethical standards and regulatory requirements for animal welfare.

References

[1] Li, G.; Pan, Q.; Zhou, Z.; Gu, R.; Zhang, H.; Huang, X.; Dong, G.; Xiao, X., Stable CsPbX3 (X = Cl, Br, I) Nanocrystal-in-Glass Composite (NGC) for Solid-State Laser-Driven White Light Generation. Adv. Opt. Mater. 11, 2203028 (2023)

[2] Pai, N.; Angmo, D., Powering the Future: Opportunities and Obstacles in Lead-Halide Inorganic Perovskite Solar Cells. Adv. Sci. 12, 2412666 (2025)

[3] Chen, S.; Lin, J.; Zheng, S.; Zheng, Y.; Chen, D., Efficient and Stable Perovskite White Light-Emitting Diodes for Backlit Display. Adv. Funct. Mater. 33, 2213442 (2023)

[4] Lin, Y.; Liu, S.; Yan, D., Flexible Crystal Heterojunctions of Low-Dimensional Organic Metal Halides Enabling Color-Tunable Space-Resolved Optical Waveguides. Research. 6, 0259

[5] Zhou, B.; Qi, Z.; Dai, M.; Xing, C.; Yan, D., Ultralow-loss Optical Waveguides through Balancing Deep-Blue TADF and Orange Room Temperature Phosphorescence in Hybrid Antimony Halide Microstructures. Angew. Chem. Int. Ed. 62, e202309913 (2023)

[6] Zhou, B.; Yan, D., Color-tunable persistent luminescence in 1D zinc–organic halide microcrystals for single-component white light and temperature-gating optical waveguides. Chem. Sci. 13, 7429-7436 (2022)

[7] Zhou, B.; Yan, D., Long Persistent Luminescence from Metal–Organic Compounds: State of the Art. Adv. Funct. Mater. 33, 2300735 (2023)

[8] Xing, C.; Zhou, B.; Yan, D.; Fang, W.-H., Dynamic Photoresponsive Ultralong Phosphorescence from One-Dimensional Halide Microrods Toward Multilevel Information Storage. CCS Chemistry. 5, 2866-2876 (2023)

[9] Chen, T.; Yan, D., Full-color, time-valve controllable and Janus-type long-persistent luminescence from all-inorganic halide perovskites. Nat. Commun. 15, 5281 (2024)

[10] Zaccaria, F.; Zhang, B.; Goldoni, L.; Imran, M.; Zito, J.; van Beek, B.; Lauciello, S.; De Trizio, L.; Manna, L.; Infante, I., The Reactivity of CsPbBr3 Nanocrystals toward Acid/Base Ligands. ACS Nano. 16, 1444-1455 (2022)

[11] Xu, K.; Allen, A. L. C.; Luo, B.; Vickers, E. T.; Wang, Q.; Hollingsworth, W. R.; Ayzner, A. L.; Li, X.; Zhang, J. Z., Tuning from Quantum Dots to Magic-Sized Clusters of CsPbBr3 Using Novel Planar Ligands Based on the Trivalent Nitrate Coordination Complex. J. Phys. Chem. Lett. 10, 4409-4416 (2019)

[12] Manna, A.; Nayek, P.; Mal, P., Tuning Dimensions of CsPbBr3 Nanocrystals through Pb(II) Counter Anions: A Dance of Dimensions and Product Selectivity in Visible-Light Photocatalysis. ACS Energy Lett. 10, 1499-1507 (2025)

[13] Soosaimanickam, A.; Adl, H. P.; Chirvony, V.; Rodríguez-Cantó, P. J.; Martínez-Pastor, J. P.; Abargues, R., Effect of alkali metal nitrate treatment on the optical properties of CsPbBr3 nanocrystal films. Mater. Lett. 305, 130835 (2021)

[14] Zheng, W.; Wan, Q.; Liu, M.; Zhang, Q.; Zhang, C.; Yan, R.; Feng, X.; Kong, L.; Li, L., CsPbBr3 Nanocrystal Light-Emitting Diodes with Efficiency up to 13.4% Achieved by Careful Surface Engineering and Device Engineering. J. Phys. Chem. C. 125, 3110-3118 (2021)

[15] Li, Z.; Goldoni, L.; Wu, Y.; Imran, M.; Ivanov, Y. P.; Divitini, G.; Zito, J.; Panneerselvam, I. R.; Baranov, D.; Infante, I.; De Trizio, L.; Manna, L., Exogenous Metal Cations in the Synthesis of CsPbBr3 Nanocrystals and Their Interplay with Tertiary Amines. J. Am. Chem. Soc. 146, 20636-20648 (2024)

[16] Zhou, Y.; Chen, J.; Bakr, O. M.; Sun, H.-T., Metal-Doped Lead Halide Perovskites: Synthesis, Properties, and Optoelectronic Applications. Chem. Mater. 30, 6589-6613 (2018)

[17] Ge, Z.; Wan, S.; Moin, M.; Moyez, S. A.; Dong, L.; Haris, H. u. R.; Piotrowski, M.; Wang, Z.; Leydecker, T.; Thumu, U., Boosting Electronic Properties of CsPbBr3 Nanocrystals via Lithium-Ion Doping and Surface Passivation for Enhanced Electrical Conductivity and Efficient White Light-Emitting Diodes. Adv. Sci. n/a, 2417304 (2025)

[18] Babeker, H.; Yang, Y.; Cao, E.; Haider, A. A.; Khan, I.; Qiu, J.; Zhou, D.; Mohammod, O., Ultrastability and color-tunability of CsPbI3 nanocrystals glass via doping CoBr2 and application in WLED. Ceram. Int. 50, 24054-24062 (2024)

[19] Wang, D.; Li, W.; Du, Z.; Li, G.; Sun, W.; Wu, J.; Lan, Z., CoBr2-doping-induced efficiency improvement of CsPbBr3 planar perovskite solar cells. J. Mater. Chem. C. 8, 1649-1655 (2020)

[20] Liu, W.-J.; Kwon, E.; Thanh, B. X.; Lee, J.; Ta, C. K.; Sirivithayapakorn, S.; Lin, K.-Y. A., Nanoscale CoNi alloy@carbon derived from Hofmann-MOF as a magnetic/effective activator for monopersulfate to eliminate an ultraviolet filter. J. Nanostruct. Chem. 14, 153-166 (2024)

[21] Liu, H.; Wang, X.; Wang, Q.; Pei, C.; Wang, H.; Guo, S., Dual-functional cobalt phosphide nanoparticles for performance enhancement of lithium-sulfur battery. J. Nanostruct. Chem. 14, 281-292 (2024)

[22] Kalita, M.; Haque, M.; Mondal, A.; Singha Roy, A., Bright Blue-Light emitting cobalt doped CuS quantum dots: Photophysical studies and selective sensing application of ferric ion. J. Photochem. Photobiol. A. Chem. 460, 116137 (2025)

[23] Cheng, J.; Mu, Y.; Wu, L.; Liu, Z.; Su, K.; Dong, G.; Zhang, M.; Lu, T., Acetate-assistant efficient cation-exchange of halide perovskite nanocrystals to boost the photocatalytic CO2 reduction. Nano Res. 15, 1845-1852 (2022)

[24] Zhang, Y.; Siegler, T. D.; Thomas, C. J.; Abney, M. K.; Shah, T.; De Gorostiza, A.; Greene, R. M.; Korgel, B. A., A "Tips and Tricks" Practical Guide to the Synthesis of Metal Halide Perovskite Nanocrystals. Chem. Mater. 32, 5410-5423 (2020)

[25] Han, X.; Wan, S.; He, L.; Zou, J.; Mavric, A.; Wang, Y.; Piotrowski, M.; Bandela, A. K.; Samorì, P.; Wang, Z.; Leydecker, T.; Thumu, U., Tunable Emissive CsPbBr3/Cs4PbBr6 Quantum Dots Engineered by Discrete Phase Transformation for Enhanced Photogating in Field-Effect Phototransistors. Adv. Sci. 11, 2401973 (2024)

[26] Vighnesh, K.; Wang, S.; Liu, H.; Rogach, A. L., Hot-Injection Synthesis Protocol for Green-Emitting Cesium Lead Bromide Perovskite Nanocrystals. ACS Nano. 16, 19618-19625 (2022)

[27] Jing, Q.; Xu, Y.; Su, Y.; Xing, X.; Lu, Z., A systematic study of the synthesis of cesium lead halide nanocrystals: does Cs4PbBr6 or CsPbBr3 form? NANOSCALE. 11, 1784-1789 (2019)

[28] Dutta, A.; Behera, R. K.; Pradhan, N., Solvent Polarity: How Does This Influence the Precursor Activation, Reaction Rate, Crystal Growth, and Doping in Perovskite Nanocrystals? ACS Energy Lett. 4, 926-932 (2019)

[29] Udayabhaskararao, T.; Houben, L.; Cohen, H.; Menahem, M.; Pinkas, I.; Avram, L.; Wolf, T.; Teitelboim, A.; Leskes, M.; Yaffe, O.; Oron, D.; Kazes, M., A Mechanistic Study of Phase Transformation in Perovskite Nanocrystals Driven by Ligand Passivation. Chem. Mater. 30, 84-93 (2018)

[30] Shukla, A.; Kaur, G.; Justice Babu, K.; Bhatt, H.; Kumar, V.; Ghosh, H. N., The Retarded Hot Carrier Relaxation and Augmented Photoconductivity in Eu3+-Doped CsPbBr3 Nanocrystals. ACS Photonics. 12, 4224-4233 (2025)

[31] Justice Babu, K.; Kaur, G.; Shukla, A.; Saha, R.; Kaur, A.; Sachdeva, M.; Yadav, D. K.; Ghosh, H. N., Fast Polaron Formation and Low Carrier Mobility in Defect-Free Polyhedral CsPbBr3 Perovskite Nanocrystals. ACS Photonics. 9, 969-978 (2022)

[32] Justice Babu, K.; Kaur, G.; Shukla, A.; Kaur, A.; Goswami, T.; Ghorai, N.; Ghosh, H. N., Concurrent Energy- and Electron-Transfer Dynamics in Photoexcited Mn-Doped CsPbBr3 Perovskite Nanoplatelet Architecture. J. Phys. Chem. Lett. 12, 302-309 (2021)

[33] Babu, K. J.; Shukla, A.; Kaur, G.; Kaur, A.; Bhatt, H.; Ghosh, H. N., Temperature-driven charge transfer process in quantum confined two-dimensional Mn-doped CsPbBr3 perovskite nanoplatelets. Chem. Commun. 58, 13899-13902 (2022)

[34] Ma, C.; Zhang, M.; Zhang, J.; Liao, J.; Sun, H.; Ji, D.; Pang, R.; Zhang, H.; Liu, J.; Liu, S., Highly Luminescent and Stable Perovskite Quantum Dots Films for Light-Emitting Devices and Information Encryption. Adv. Funct. Mater. 34, 2316717 (2024)

[35] Zhang, Y.; Li, H.; Han, L.; Xu, Y., Engineering Green-to Blue-Emitting CsPbBr3 Quantum Dots in Nanozeolite with High Stability for Backlight Display Application. Nano Lett. 24, 16400-16407 (2024)

[36] Yu, M.; Xu, Y.; Lin, J.; Yu, C.; Fang, Y.; Liu, Z.; Guo, Z.; Tang, C.; Huang, Y., Compression packing of CsPbBr3 perovskite quantum dots with boron nitride nanosheets for enhanced stability: A nano-encapsulation strategy. Appl. Surf. Sci. 610, 155585 (2023)

[37] Xu, Y.; Li, W.; Hu, Q.; Wu, H.; Guo, Y.; Jiang, F.; Feng, G.; Zhang, X.; Wang, S.; Wang, L.; Jiang, W., Dual-shell protection enables highly efficient and stable all-inorganic perovskite composites for light-emitting-diodes. J. Alloys Compd. 1010, 177135 (2025)

[38] Lee, W.; Li, H.; Wong, A. B.; Zhang, D.; Lai, M.; Yu, Y.; Kong, Q.; Lin, E.; Urban, J. J.; Grossman, J. C.; Yang, P., Ultralow thermal conductivity in all-inorganic halide perovskites. PNAS. 114, 8693-8697 (2017)


Co:CsPbBr3
WLED
Br⁻
CH3COO⁻
NO3⁻
Co:Cs4PbBr6NCs
Cs⁺:PbBr2:CoX2 (X=Br⁻,NO3⁻,CH3COO⁻)